THE JOURNAL OF PHYSICAL CHEMISTRY C

Article

pubs.acs.org/JPCC

Diffusion-Recombination Determines Collected Current and Voltage in Polymer:Fullerene Solar Cells

Teresa Ripolles-Sanchis, Antonio Guerrero, Juan Bisquert, and Germà Garcia-Belmonte*

Photovoltaic and Optoelectronic Devices Group, Departament de Física, Universitat Jaume I, ES-12071 Castelló, Spain

ABSTRACT: The basic operating mechanisms of organic bulk-heterojunction cells comprising poly(3-hexylthiophene (P3HT): [6,6]-phenyl-C_{61}-butyric acid methyl ester (PCBM) blends are examined based on the selection of diverse materials as cathode contact. The use of both highly and poorly efficient cathodes in combination with impedance spectroscopy allows for a clear-cut separation of the physical mechanisms occurring within the active layer bulk from those taking place at the organic blend-contact interface. The system under study uses either Ca or CaO as the efficient and blocking contact, respectively. The impedance analysis demonstrates that charge carriers (electrons) move by diffusion within extended quasi-neutral regions, so that the cell operation is governed by the kinetic competition between charge transport toward the outer contacts and loss by recombination. It is also observed that contacts contribute with an additional, non-negligible, series resistance that accounts for the electron extraction process. The comparison between active layer thickness and the carrier diffusion length allows exclusion of bulk transport losses as a highly detrimental factor for this class of solar cells.

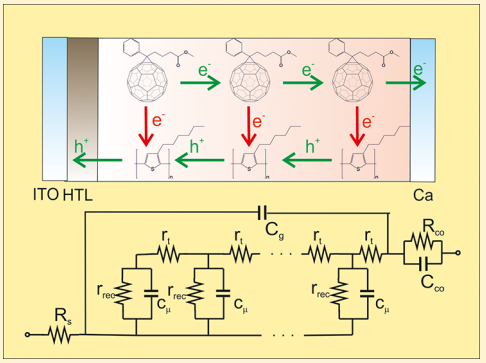

1. INTRODUCTION

In the pursuit for engineering versatile and cheap light-harvesting solar cells, organic solar technologies have demonstrated in the past few years their ability to reach competitive levels of power conversion efficiency (PCE). Innovations in materials design (i.e., low bandgap polymers or use of additives) and cell architectures (i.e., incorporation of carrier selective interlayers or a better blend morphology control) have allowed achieving over 10% in PCE.[1] Further performance improvements might result from a detailed understanding of the loss mechanisms reducing PCE. In addition to phenomena determining charge photogeneration, deeper knowledge about processes governing charge carrier motion, recombination, and outer interface charge selection and extraction might become crucial. Particularly important is the overall impact of the electronic transport mechanisms, which have dramatic effects when relatively thicker active layer films are used to enhance light harvesting. Thinner films are usually able to exhibit almost 100% conversion of absorbed photons into collected carriers,[2] thus indicating that transport mechanisms do not limit the achievable photocurrent.[3] Most thicker active layer devices suffer from an incomplete collection of photogenerated charges as recombination processes have sufficient time to affect charges being transported. This last statement is however not general as demonstrated with some polymer:fullerene combinations.[4] Therefore, quantifying the influence of competing carrier transport and recombination mechanisms[5,6] on cell performance has become a major topic for organic bulk-heterojunction photovoltaics.

The clarification of the presence or absence of extended quasi-neutral regions within the active layer bulk is a central point prior to establishing the basics of device physics for organic bulk-heterojunction solar cells. If quasi-electroneutrality is invoked, then even in the case of current flow space charge regions related to excess carriers cannot be built up, and the analytical treatment of the mathematical system describing the solar device is considerably simplified.[7] The dielectric relaxation time is related to the material permittivity $\varepsilon\varepsilon_0$ (ε being the dielectric constant, and ε_0 the vacuum permittivity), and its conductivity σ is as follows:

$$\tau_{die} = \frac{\varepsilon\varepsilon_0}{\sigma} \quad (1)$$

The assumption of the occurrence of quasi-neutral regions relies on the property that carrier lifetime (recombination time, τ_{rec}) is much larger than the dielectric relaxation time τ_{die}. If $\tau_{rec} > \tau_{die}$ mobile carriers can exist long enough to neutralize charge. Depending on whether $\tau_{rec} > \tau_{die}$ (*lifetime* semiconductor regime), or $\tau_{rec} < \tau_{die}$ (*relaxation* semiconductor regime), the physics governing the device operation changes drastically. In the relaxation semiconductor regime, electroneutrality is not a justifiable assumption. Hence regions of near-zero net local recombination may occur, implying spatially separated excess electron and hole concentrations. This will enhance the space charge of dielectric relaxation-dependent decay.[8] For instance, low-conductivity amorphous *p-i-n* silicon solar cells were modeled as developing photogenerated hole space charge regions near the *p* contact that concentrate the voltage drop.[9] In the extreme case, currents should be space charge limited as

Received: June 16, 2012
Revised: July 21, 2012
Published: July 23, 2012

occurring in organic light-emitting diodes based on low-mobility polymers or molecules.[10]

In order to classify the solar cell blend as operating within the relaxation ($\tau_{rec} < \tau_{die}$), or lifetime ($\tau_{rec} > \tau_{die}$) regime, the polymer conductivity plays a crucial role, as derived from eq 1. It has previously been established that many polymers used for photovoltaic applications contain native carriers due to doping, normally of p-type.[11] The archetypical regioregular poly(3-hexylthiophene) (P3HT) is known to have a background hole density of order $p_0 \approx 10^{16}$ cm^{-3},[12,13] which taking into account the reported mobility ($\mu_h \approx 10^{-4}$ cm^2 V^{-1} s^{-1}) in diode configuration,[14,15] the relationship $\sigma = q\mu_h p_0$ and typical permittivity values for this compound ($\sim 3\varepsilon_0$) yields a value for the relaxation time of $\tau_{die} \leq 1$ μs. Typical recombination times experimentally found approaching open-circuit voltage V_{oc} at 1 sun irradiation intensity, by using different methods, are on the order $\tau_{rec} \approx 10$ μs.[16,17] A device will then be operating in lifetime or relaxation regime depending on the materials properties. Indeed, many active layer blends can be viewed as a specific case of lifetime semiconductors. We have suggested that the depletion region built up in the vicinity of the cathode contact, collapses at forward bias giving rise to extended quasi-neutral regions in organic photovoltaic device.[18,19] Depletion region modulation (spatially confined band bending) by the applied voltage has been identified using alternative methods.[13,20,21]

Since the depletion zone is reduced or even eliminated at operation voltages close to the maximum power point (flatband voltage lies in the range of 0.4 V in most cases), there remains the neutral region in which transport of minority carrier should be controlled by diffusion[22] while the high conductivity of majority carriers (holes) assures rapid shielding. So far, however, observation of the diffusive transport that is clearly predicted by this device model has been elusive, due to other experimental aspects that interfere with the diffusion signatures.

This work aims to show evidence for the first time of the existence of diffusion currents governing the electronic transport at forward bias voltages between maximum power point and V_{oc} in the case of P3HT:PCBM-based cells. It is observed by means of impedance spectroscopy methods that typical diffusive impedance patterns (Warburg response) occur either at large bias voltage for working bulk-heterojunction solar cells, or using devices in which a blocking layer has been inserted between the active layer and cathode contact. Moreover, the analysis incorporates all relevant mechanisms which are expected to intervene within the active layer bulk, namely: carrier transport, recombination current, and charge storage. The impedance response is modeled by means of transmission line models previously introduced in analyzing electron diffusion and recombination in thin layers[23] and later for organic solar cells.[18]

Finally, by altering the structure of the cathode contact, we have identified and modeled the effect of the outer interfaces.[24,25] Two different cathodes (electron extracting or blocking layer) have allowed the observation of the additional resistive and capacitive responses occurring at the interface that have a significant effect on the measured current−voltage characteristics (j-V). A complete small-amplitude electrical model is presented which permits a fine analysis of determining physical processes taking place in operating devices.

2. EXPERIMENTAL SECTION

2.1. Device Fabrication. P3HT (Aldrich), PEDOT:PSS (CLEVIOS P AI 4083), o-dichlorobenzene (Aldrich, 99.9%), Ca (Aldrich, 99.995%) and silver (Aldrich,99.99%) were used as received without further purification. All manipulations were carried out in a glovebox under a nitrogen atmosphere unless otherwise stated. P3HT:PCBM blends (1:0.8) were prepared from dry o-dichlorobenzene and were stirred at R.T. for 24 h prior to device fabrication. Concentrations based on P3HT of 17 mg/mL were used to obtain active layer thickness of ∼110 nm.

Polymer solar cells were fabricated using a standard sandwich structure of ITO/PEDOT:PSS/P3HT:PCBM/Cathode, and 9 mm^2 of active area (cathode = Ca/Ag or CaO/Ca/Ag). Precleaned ITO coated glass substrates (10 Ω/sq) were treated in a UV−O_3 chamber for 5 min followed by the deposition of PEDOT:PSS by spin coating in air at 5500 rpm for 30 s, film thickness of ∼35 nm. The substrates were heated at 120 °C for 10 min to remove traces of water and were transferred to a glovebox equipped with a thermal evaporator. The P3HT:PCBM layer was deposited at speeds of 1200 rpm (thickness was about 110 nm) for 20 s followed by a slow drying process in a petry dish to provide a dry film. For cells requiring the blocking layer a layer of calcium was evaporated to the desired blocking layer thickness. The evaporated Ca was oxidized using ambient conditions overnight. At this point, all samples were thermally annealed at 130 °C for 10 min to provide an adequate morphology and to promote oxygen desorption. Evaporation of the finished contact was carried out at a base pressure of 3×10^{-6} mbar with Ca/Ag (5/100 nm). Devices were encapsulated with a photoresin and a glass microscopy slide followed by exposure under UV light. Samples were then taken out of the glovebox for device characterization.

2.2. Device Characterization. Current density−voltage and impedance spectroscopy measurements were carried out by varying irradiation intensity (1.5G illumination source 1000 W m^{-2}) using an Abet Sun 2000 Solar Simulator. The light intensity was adjusted with a calibrated Si solar cell. Impedance spectroscopy measurements were performed with Autolab PGSTAT-30 equipped with a frequency analyzer module, and was recorded by applying a small voltage perturbation (20 mV rms). Measurements were carried out at different light intensity and bias voltage sweeping frequencies from 1 MHz down to 100 Hz. The light intensity was measured using an optical power meter 70310 from Oriel Instruments, where a Si photodiode was used to calibrate the system. Direct determination of the relaxation time was performed by transient photocurrent experiment TPC by connecting the devices to a low input (50 Ω) impedance oscilloscope (Agilent 500 MHz bandwidth) which allows measuring near short-circuit conditions. A nitrogen pumped-dye pulsed laser of 596 nm wavelength and 5 ns pulse duration was used to generate a small light perturbation.

3. RESULTS

The device structure used in this work is based on a sandwich structure of indium tin oxide (ITO)/poly(3,4-ethylenedioxythiophene): poly(styrene sulfonic acid) (PEDOT:PSS)/poly-(3-hexylthiophene) (P3HT): [6,6]-phenyl-C_{61}-butyric acid methyl ester (PCBM)/Cathode, (cathode = Ca/Ag or CaO/Ca/Ag). Active layer thickness is situated around 100 nm. Structures used are schematically drawn in Figure 1(a). With

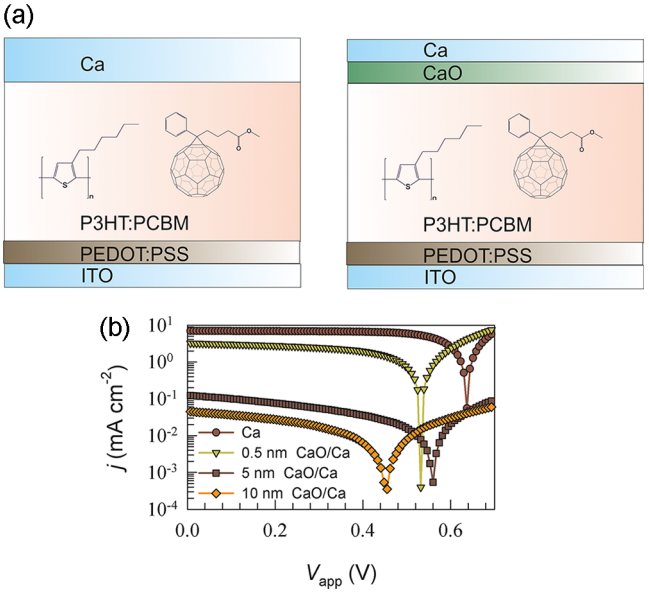

Figure 1. (a) Device configuration of analyzed bulk-heterojunction devices: ITO/PEDOT:PSS/P3HT:PCBM/cathode. Two different cathodes are used: efficient collecting contact based on Ca and insertion of an oxide layer (CaO) of different thickness that blocks the electron collection. (b) $j-V$ curves under 1 sun illumination corresponding to devices using different cathode contact structures. The oxide layer thickness is indicated, ranging from 0.5 to 10 nm.

the aim of studying transport mechanisms under conditions of suppression of dc current flux, a blocking cathode contact has been tested by including CaO layers of different thickness. For thicker oxide layers (10 nm), a complete electron blockage is observed. As we will next explain, blocked cells let us probe the internal electron motion under illumination without the perturbing influence of dc current flowing.

3.1. Effect Blocking Contacts. Figure 1(b) represents $j-V$ characteristics under 1.5G illumination (1000 W m^{-2}) of cells comprising the same organic blend but different cathode contact structure (Table 1). The dramatic effect that the CaO layer produces on the achievable photocurrent is evident in Figure 1(b). As the oxide layer thickness grows, j_{sc} is severely limited by blocking the extraction of photogenerated electrons at the cathode contact. Noticeably, the blocking effect accounts for a reduction of more than 2 orders of magnitude in j_{sc}, while the open-circuit voltage V_{oc} is only reduced by ~200 mV. This last observation suggests that blocked devices under steady-state illumination do not loss completely their ability to accumulate photogenerated carriers despite the oxide layer located at the cathode contact. This occurs because V_{oc} monitors in fact the Fermi level splitting of separated charge carriers in the blend material $qV_F = E_{Fn} - E_{Fp}$, which are ultimately governed by the electron and hole occupancy of their respective electronic states. The electron Fermi level equilibrates with the cathode metal then producing the measured output voltage despite the presence of the oxide layer.

A close look at the impedance response of blocked solar devices (with 10 nm-thick CaO layer) let us corroborate that the charge carriers are being stored as suggested previously. Figure 2(a) shows the evolution of the capacitance spectra $C-f$ measured in open-circuit upon variation of the light intensity from dark conditions until nearly 1 sun. Dark capacitance exhibits the expected flat value originated from the dielectric response of the active layer (geometrical capacitance C_g). As the illumination is raised up, capacitance develops a plateau within the frequency range between 100 Hz–1 kHz which signals to the accumulation of excess photogenerated charge

Table 1. Device Operation Parameters under 1.5G Illumination Source (1000 W m^{-2}) for the Devices with P3HT:PCBM Active Layer Using Different Cathodes, Ca/Ag, and Different Blocking Layer (CaO) Thicknesses: 0.5 nm, 5 nm, and 10 nm in CaO/Ca/Ag Cathodes[a]

		j_{sc} (mA cm^{-2})	V_{oc} (mV)	FF	PCE (%)
P3HT:PCBM cathode Ca/Ag		7.0	636	0.67	2.94
P3HT:PCBM cathode CaO/Ca/Ag	CaO (0.5 nm)	3.2	531	0.46	0.79
	CaO (5 nm)	0.1	550	0.24	0.02
	CaO (10 nm)	4×10^{-2}	449	0.28	0.01

[a]Average values shown with variations below 10% for different samples.

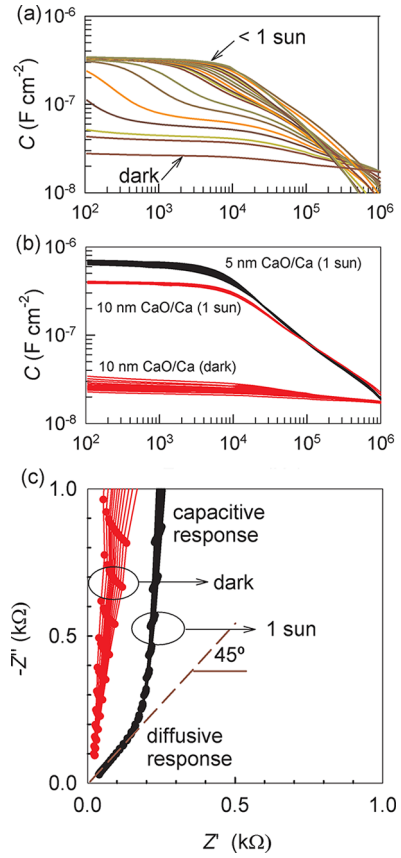

Figure 2. (a) Capacitance spectra plots of a device blocked with CaO (10 nm) measured at different light intensities from the dark to nearly 1 sun illumination, and zero bias. (b) Capacitance spectra plots of devices blocked with two different CaO layer thicknesses measured under 1 sun illuminations and in the dark. At each condition, the applied voltage is varied within the range of −1 to 1 V. Note here the small variation introduced by the bias voltage. (c) Impedance spectra comparison of the impedance plot measured under 1 sun illumination (right spectra) and dark conditions (left spectra) of a device blocked with CaO (10 nm). Applied voltage is varied as in (b).

dx.doi.org/10.1021/jp305941f | J. Phys. Chem. C 2012, 116, 16925–16933

carriers. The total increase in capacitance over C_g amounts to more than 1 order of magnitude as observed in Figure 2(b) that compares dark and light (1 sun) responses under variation of the applied voltage. Interestingly, the reached low-frequency capacitance appears not to be very sensitive to the bias voltage. This occurs because the external voltage is unable to modify the internal photogenerated V_F and mainly drops at the huge series resistance introduced by the oxide layer. We checked that the low-frequency capacitance plateau is determined by the CaO layer thickness giving larger values of C_{ox} for thinner oxide layers, as shown in Figure 2(b). This last finding helps us to identify C_g and C_{ox} as the limiting capacitances at low (dark) and high illumination conditions. The chemical capacitance C_μ, originated by the storage of photogenerated charges,[19,26] increases with increasing the irradiation intensity and is observed in the middle frequency range. We note here that oxide layers have also been used in MOS structures to investigate the quantum (chemical) capacitance of graphene sheets, in which the graphene capacitance is connected in series with the gate capacitance,[27] similar to the effect found here.

The previous results account for the basic capacitive phenomenology as extracted from the low-frequency part of the spectra. The resistive component at low frequencies exhibits a huge resistor in accordance with the current limiting effect observed in Figure 1(b). By looking at the high-frequency response (f > 10 kHz), the behavior changes radically. Instead of purely capacitive spectra, a clearly distinguishable diffusion pattern is observed in Figure 2(c) for illuminated samples. Impedance spectra ($Z''-Z'$) is selected now to make evident the diffusive mechanism fingerprint as a 45°-slope caused by the coupling of diffusive transport and chemical capacitance (Warburg response). Such a coupling of transport and charge accumulation mechanisms is described by standard impedance model functions[23] and it is often useful to represent the model in terms of distributed element circuits (transmission lines) as discussed later. Note that the response is still basically capacitive in the dark, as observed by the nearly vertical responses in Figure 2(c), but this behavior shifts to diffusive only when excess photogenerated charges are created. Interestingly, the effect of illumination is totally decoupled from the bias voltage influence for blocked devices, as deduced form the similar response found by variation of V_{app}.

3.2. Response of Working Devices. It is interesting to compare the above presented results of devices incorporating CaO layers with those yielded by good extracting contacts as Ca metal. We stress here that the only modification now with respect to the blocked devices is that the blocking layer is not present, leaving the rest of the cell unaltered. In this case, similar bulk mechanisms are then expected. However, contrary to the complete decoupled effect of light and applied voltage observed for blocked devices, it has been demonstrated that sufficiently thin active layers and good extracting contacts ensure electronic reciprocity[28] (i.e., voltage and local charge density are univocally determined).[3] If electronic reciprocity is obeyed, then the same charge density is obtained either as photogenerated charges (producing certain photovoltage) or injected charges (caused by an applied voltage) when V_{app} and the photovoltage attain the same value. One can infer by examining Figure 3(a) that the applied bias voltage has a great influence on low-frequency capacitance because now charge carriers are injected from the contacts. A similar effect producing a rise in capacitance is observed when devices are

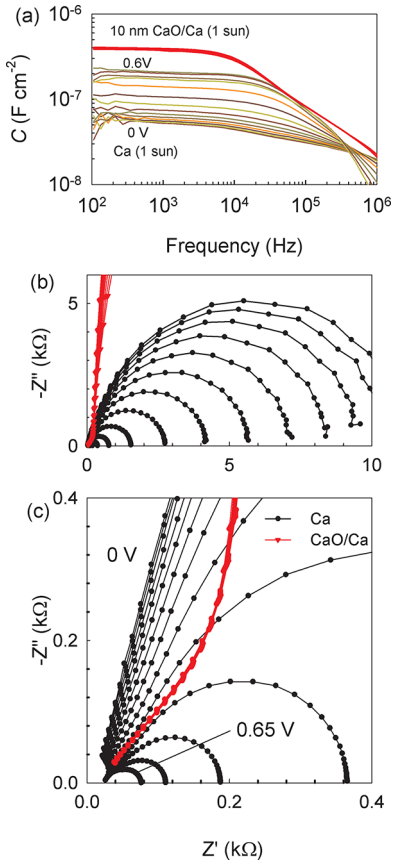

Figure 3. Impedance response from devices using either a good electron collector (Ca) or a blocking layer (CaO). (a) Capacitance spectra measured under 1 sun illumination by varying the applied voltage between 0 and 0.6 V. (b) Impedance spectra plots measured at 1 sun light intensity showing features at low frequencies: recombination *RC* arc for extracting contacts, and capacitive behavior for blocking contacts. (c) Detail of the high frequency region: a transition is observed between spectra dominated by the geometrical capacitance (low bias voltage) and diffusion patterns at high bias near open circuit voltage.

measured at different illumination intensities in open-circuit conditions (not shown).

The impedance response of working bulk heterojunction solar cells has been summarized in previous reports.[29] We usually observed that the impedance spectra comprise two visually distinguishable parts. At lower frequencies, a large parallel *RC* subcircuit (represented by a semicircle in $Z'-Z''$ plot) dominates as observed in Figure 3(b). This part is related to the chemical capacitance C_μ (connected to carrier storage) and recombination resistance R_{rec} (derivative of the carrier recombination flux) response,[17,30−33] and kinetic recombination parameters such as the lifetime τ_{rec} can be extracted from this information. At higher frequencies, and bias voltages approaching V_{oc} spectra are usually more featured, exhibiting in some cases an additional arc. Figure 3(c) shows a comparison between electron blocking and extracting solar cells. As we will explain later, the high-frequency part changes from being purely capacitive C_g at low forward bias to diffusive at high forward bias.

4. TRANSMISSION LINE MODEL

A general model accounting for the different impedance responses valid for both blocked and working devices is

dx.doi.org/10.1021/jp305941f | J. Phys. Chem. C 2012, 116, 16925−16933

desired as this can provide quantitative information on the different physical processes taking place in an operating cell. In order to obtain such a model, a series of separated mechanisms need to be considered: (i) Geometrical capacitance C_g is observed under some experimental conditions (low voltage for Ca cathode, and dark for CaO contacs). (ii) Blocking effect is clearly visible for blocking contacts (CaO). This implies an *RC* parallel subcircuit connected in series $R_{co}C_{co}$ that must comprises large resistances in the case of oxide layers $R_{co} = R_{ox}$, but much smaller for extracting contacts. (iii) For Ca contacts (working devices), the recombination subcircuit is clearly distinguishable $R_{rec}C_{\mu}$. And finally (iv) diffusion patterns are dominant at high frequencies, more evident in the case of blocked devices as a Warburg response. Integration of points (iii), and (iv) electrical mechanisms relies on regarding equivalent circuits comprising distributed elements, which are usually drawn in terms of transmission line models. This type of impedance pattern belongs to responses usually encountered in systems in which carrier transport is determined by coupled diffusion-recombination.[23] Minority carriers (electrons) are able to diffuse within extended bulk neutral regions eventually reaching the electrodes which act as selective contacts. Transmission line models able to represent such diffusion-recombination impedance response are well-known,[23,34] and have been integrated in standard software so that fitting the impedance spectra to obtain the model parameters is straightforward. The impedance model in Figure 4(a) consists of an equivalent circuit which comprises:

- Distributed resistors $r_t = R_t/L$ (being L the active layer thickness), standing for the electron transport. r_t is the reciprocal of the electron conductivity σ_n,
- Distributed chemical capacitance $c_{\mu} = C_{\mu}L$, and
- $r_{rec} = R_{rec}/L$ accounting for the electron recombination resistance.

Since holes are regarded as majority carriers (a hole background density exists in the dark) an equipotential line suffices to represent their contribution because of the sufficiently high conductivity of the materials, provided that the lifetime regime ($\tau_{rec} > \tau_{die}$) is satisfied as previously discussed. The impedance model described contains two characteristic times related to the electron diffusion (transit time),

$$\tau_{diff} = R_t C_{\mu} \quad (2)$$

and the effective lifetime,

$$\tau_{rec} = R_{rec} C_{\mu} \quad (3)$$

respectively.[23] It is assumed that distributed (differential) circuit elements are position-independent as expected for cells in which recombination is not severe, i.e., $\tau_{diff} \leq \tau_{rec}$ (or $R_t \leq R_{rec}$). For highly recombining devices ($\tau_d > \tau_{rec}$ or $R_t > R_{rec}$) deviations from the Warburg response at high-frequencies are usually observed.[34] An additional series resistance is needed to model contact and wire effects, R_s. The electrical effect of the cathode contact is modeled by means of $R_{co}C_{co}$ parallel subcircuit connected in series with the electron channel. Finally, a capacitor $C_g = \varepsilon\varepsilon_0/L$ represents dielectric, geometrical capacitance of the active layer bulk.

The equivalent circuit in Figure 4(a) incorporates the basic phenomenology reported on the impedance response of blocked and working devices as explained in previous sections. Additional assumptions incorporated in the model should be also mentioned: the ohmic character of the anode contact, and the absence of frequency-dispersion in modeling transport properties. As an example of the fitting ability, Figure 4(b) draws the comparison between experimental data and fits corresponding to two particular impedance responses. For blocked solar cells under illumination, two visible features are well supported by the equivalent circuit: the diffusion pattern (Warburg response) at high-frequencies appears as a consequence of the transport R_t and charge storage C_{μ} coupling. The low-frequency part is dominated by the contact subcircuit $R_{co}C_{co}$, which in this case draws a large arc because of the huge blocking resistor $R_{co} = R_{ox}$. In the case of working devices, the electron blocking effect is not viewed because $R_{co} \ll$ in such a way that the low-frequency response becomes governed through recombination mechanisms modeled by coupling of the parameters R_{rec} and C_{μ}. It is worth noting that at forward bias below V_{oc} [0.50 V as illustrated in Figure 4(b)] the diffusion pattern is clearly recovered. For lower voltages [see Figure 3(c)], the high frequency response turns to be dominated by the geometrical capacitance. A fitting procedure was checked by evaluating *F* statistics. Confidence intervals and correlation between parameters both provide a discriminating tool for stating the best set of fitting parameters. Confidence levels are in all cases high enough (>99%) to consider the parameter values, a very good estimation of the model quantities. In all cases, the regression coefficient of fits $r^2 >$

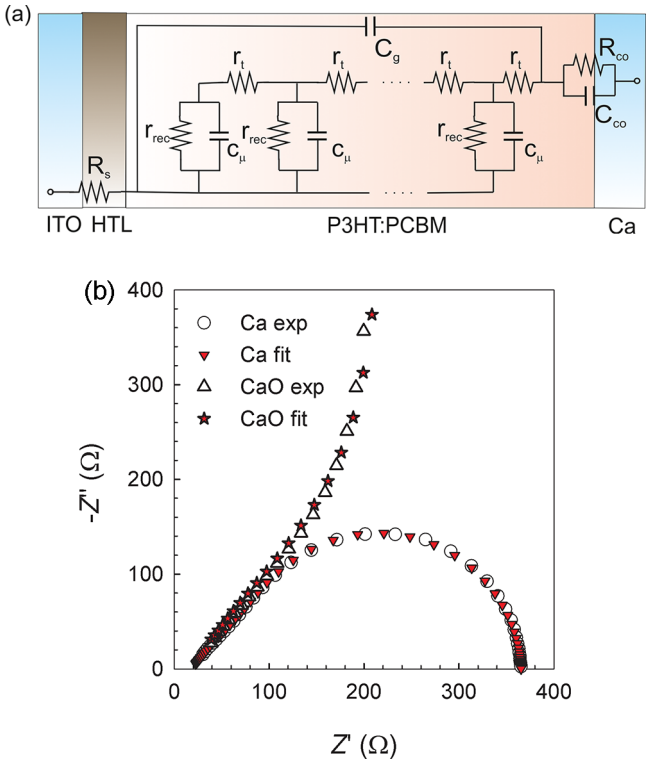

Figure 4. (a) The equivalent circuit (transmission line model) used in this work comprising circuit distributed elements related to electron transport r_t, recombination r_{rec}, chemical capacitance c_{μ}. In addition, geometrical capacitance, C_g, and series resistance, R_s, are connected to the transmission line. Contact electrical response is modeled by means of $R_{co}C_{co}$ parallel subcircuit. (b) Impedance response measured under 1 sun illumination at high frequencies for blocked (10 nm CaO) and operating devices (Ca cathode) at 0.50 V applied voltage. Comparison between experimental data and fitting is shown. Parameter errors are always below 5%.

dx.doi.org/10.1021/jp305941f | J. Phys. Chem. C 2012, 116, 16925−16933

0.995. The combination of these statistics (namely the dependences between parameters, confidence levels, and regression coefficients) signals the high accuracy that can be reached using the circuit model of Figure 4(a). Resulting errors bars are always below 5% of the parameter value.

5. ANALYSIS OF FITTING PARAMETERS

5.1. Resistive Elements. We discuss the interpretation of parameters extracted from fitting of the equivalent circuit model in Figure 4(a) to impedance data collected under 1 sun irradiation intensity by varying bias voltage. Figure 5 shows the

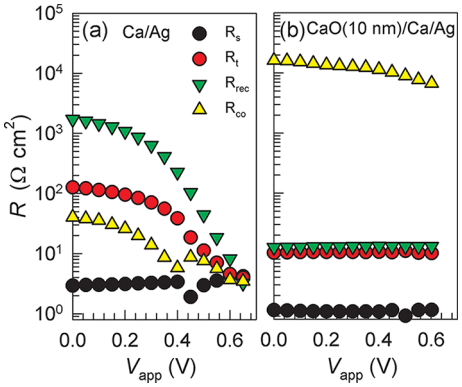

Figure 5. Resistance values extracted from fitting the circuit model in Figure 4(b) to impedance spectra of a device P3HT:PCBM-based device using extracting contacts with Ca (a), and a device blocked with 10 nm of CaO (b). Error bars (<5%) are omitted because smaller than the dot size.

four types of resistive effects that contribute to the cell operation. Low series resistances R_s = 1−3 Ω cm^2 are found that are related to conductive ITO and PEDOT:PSS layer electrical response. Contact resistance R_{co} changes by orders of magnitude between blocking (including CaO), and extracting cathodes. It is worth noting that our method is able to detect contact resistance contributions *even in the case of working devices*, which is a rather significant aspect for practical implementation of the technology. The overall series resistance is $R_s + R_{co}$, these are the conduction processes connected in series with the internal photovoltaic effect. As in the case of including a CaO layer the total series resistance is so pronounced, the voltage drop at short-circuit conditions calculated as $j_{sc}R_{co}$ amounts ∼500 mV, a value that approaches V_{oc}. This can be interpreted by considering that upon light exposure blocked cells are able to store similar photogenerated charge carrier densities regardless of the applied voltage, as this is mainly absorbed within the oxide layer. In open-circuit conditions, the voltage drop in series vanishes in such a way that a measurable photovoltage appears as $V_{oc} = V_F$.

The opposite device operation is encountered for extracting contacts: since the total series resistance is low, the applied voltage establishes the internal V_F. We have recently observed that P3HT-based solar cells operate under the electronic reciprocity relationship.[28] Under this principle, the voltage (Fermi level splitting) V_F fixes the local charge density, and the solar cell operation is viewed as a balance between voltage-independent photocurrent and illumination-independent recombination current.[3]

R_{rec} follows the expected behavior decreasing toward forward voltage due to the enhancement of the recombination current. A detailed analysis of the recombination process from R_{rec} has recently been reported.[35] We note here that the transport (diffusive) resistance, R_t, also describes a reduction at forward bias because of the increment in carrier density as we explain later. It is also interesting to point out that for blocked cells, R_{rec} and R_t exhibit rather voltage-independent values. Such values correspond to those encountered with working cells at $V_{app} \approx$ 500 mV, again indicating the state of charge reached under illumination using blocking oxide layers.

5.2. Capacitive Elements. A comparison of the capacitive parameters between blocking and working cells extracted from impedance fitting can be viewed in Figure 6. By using Ca

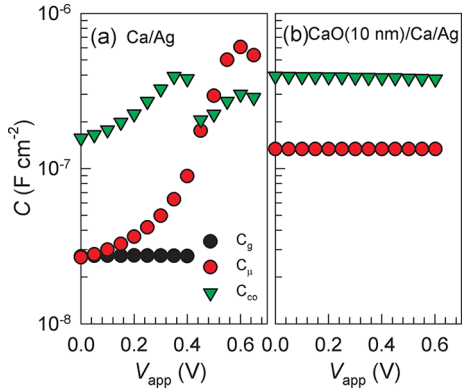

Figure 6. Capacitance values extracted from fitting the circuit model in Figure 4(b) to impedance spectra of a device P3HT:PCBM-based device using extracting contacts with Ca (a), and a device blocked with 10 nm of CaO (b). Error bars (<5%) are omitted because smaller than the dot size.

cathode metal, it is observed that C_g exerts an influence on the high-frequency part of the spectra in the low forward bias region as commented upon before in Figure 3(c). The chemical capacitance, C_μ, exhibits the expected increase as fullerene states are occupied toward forward bias. Interpretation of C_μ in terms of the electron density-of-states DOS has been discussed extensively in previous papers.[17,29] It is worth noting here that C_μ shows a voltage-independent value for blocked cells which approximately corresponds to the chemical capacitance found for working cells at $V_{app} \approx$ 500 mV. As discussed in comparing the resistances of blocked cells reach a certain degree of photogenerated charge storage that is responsible for the measured output voltage V_{oc}. The capacitive effect of the cathode contacts C_{co} can be extracted by fitting the response of both types of photovoltaic devices. For blocked cells, this capacitive value coincides with that measured in the low-frequency regime as observed in Figure 2(b). One can directly connect $C_{co} = C_{ox}$ as the values scale with the oxide layer thickness. A value for the dielectric contact of CaO is calculated to be $\varepsilon = 4.2 \pm 0.2$, in good agreement with reported values for this oxide.[36,37] However, in the case of working devices, a contact capacitance is also observed within the same order of magnitude. Such capacitance might be originated by dielectric mechanisms occurring at the interface as those recently proposed in analyzing the cathode equilibration.[25] Reduced fullerene molecules in close contact to the metal contact form a dipole layer with an accumulated charge that follows the interfacial density-of-states IDOS g_{is}. Because it is assumed that the IDOS directly equilibrates with the Fermi level of the contacting metal, one can straightforwardly derive that C_{co} =

dx.doi.org/10.1021/jp305941f | J. Phys. Chem. C 2012, 116, 16925−16933

qg_{is}. Using the extracted value of $C_{co} \approx 3 \times 10^{-7}$ F cm^{-2}, a surface state density $g_{is} \approx 3 \times 10^{12}$ cm^{-2} eV^{-1} is encountered. We note here that IDOS values within the range of 10^{12}–10^{14} cm^{-2} eV^{-1} have been calculated by other authors using alternative methods.[38]

5.3. Diffusion Coefficient. The electron diffusivity (chemical diffusion coefficient) can be calculated by recalling eq 2 through the relationship:[39]

$$D_n = \frac{L^2}{\tau_{diff}} \tag{4}$$

Here, $L \approx 100$ nm corresponds the thickness of the diffusion zone (active layer thickness). It is shown in Figure 7 that the diffusion coefficient derived from eq 4 in the case of blocked devices with 10 nm-thick CaO layer, and working solar cells. In this last type of device, D_n exhibits a rather constant value that starts to slightly increase for voltages approaching V_{oc}. A similar slight increment in D_n was identified using other polythiophene derivatives in an electrochemical transistor setup.[40] Differences in D_n between both types of cells (blocking and working) can be readily assigned to experimental errors related to the active layer thickness determination. Although the electron statistics depart from dilute concentration conditions (Boltzmann approximation), an estimation for the electron mobility might be calculated by using the Nernst–Einstein relationship as $\mu_n = qD_n/k_BT$ (k_BT being the thermal energy).[40,41] The electron mobility extracted from fits exhibits a value approximately equal to 2×10^{-3} cm^2 V^{-1} s^{-1}. This value is in good agreement with that derived using PCBM electron-only devices from J–V measurements, for which current is considered space-charge-limited, and hence electrical field-driven rather than diffusion-determined.[42] Also the time-of-flight current transient response of thick devices has provided similar values.[13]

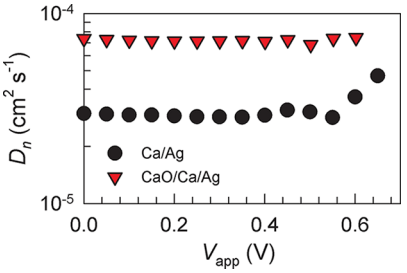

Figure 7. Diffusion coefficient as a function of the applied bias of working and blocked devices with 10 nm of CaO. Variation of layer thickness of 10% allows explaining differences in values extracted from different cells.

6. DISCUSSION

Analysis of the impedance response of working (extracting Ca cathode metal) and blocking (CaO interlayer) solar cells devices clearly shows that extended quasi-neutral regions dominate the device operation for a significant range of applied voltages. This voltage range appears in excess of that (flat-band voltage) established by the collapse of the depletion region formed in the vicinity of the cathode contact.[19] A general picture on the operation of bulk-heterojunction solar cells arises from our experiments: In open-circuit conditions [Figure 8(a), (b)], the internal voltage V_F arising from the splitting of the Fermi levels is fully determined either by the applied voltage or the irradiation intensity (as stated by electronic reciprocity

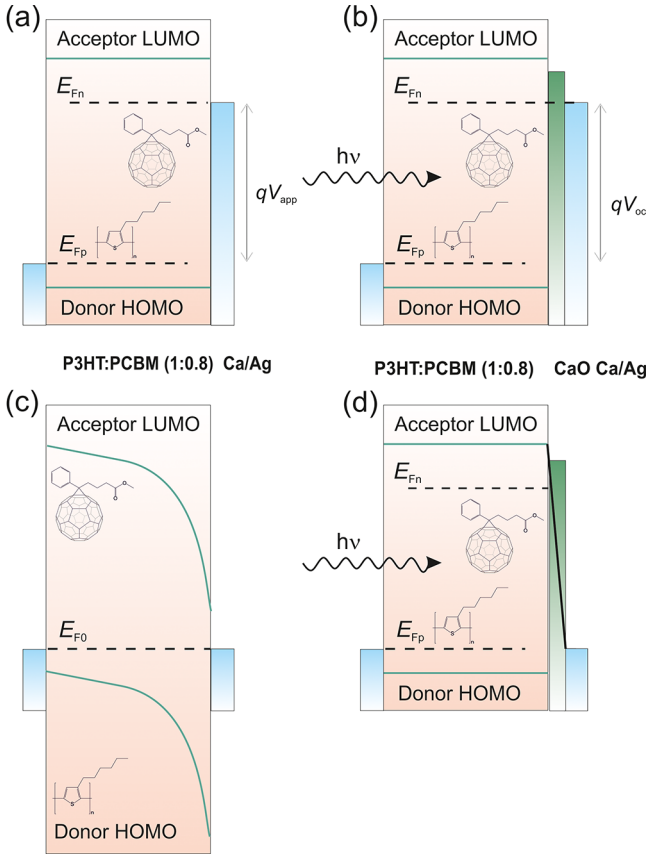

Figure 8. Band diagram of working device with collecting Ca cathode contacts at large forward applied voltage (a) and short-circuit conditions (c). The applied voltage generates the splitting of the Fermi levels, which align with the contacts producing flat-band conditions (a). Band bending resulting from the cathode Schottky contact (c). For blocking contacts (CaO layer) under illumination photogeneration creates a photovoltage (open-circuit conditions) by alignment of the respective Fermi levels (b). In short-circuit (d), a large voltage drop is confined within the oxide layer that compensates the photovoltage.

principle) only in the case of good extracting contacts. For blocked devices, light and applied voltages are completely decoupled so that only illumination is able to promote electrons into fullerene acceptor states yielding measurable values for V_F. This last fact occurs because the Ca cathode metal work function is in intimate contact with the electron Fermi level within the active layer bulk. The enormous resistance associated to the oxide layer absorbs the applied voltage impeding the Fermi level rise. When devices are forced to operate in short circuit conditions, the impedance of blocked cells does not change significantly since the internal photogenerated charge density keeps the values reached in open-circuit (voltage-independent response) as illustrated in Figure 8(d). We note that in the previous cases, devices can be viewed as operating in flat-band conditions. On the contrary, working cells under short-circuit conditions exhibits some kind of band bending because of the presence of cathode depletion zones as illustrated in Figure 8(c).

From the analysis of the resistive circuit elements, it turns out that $R_t \leq R_{rec}$ as plotted in Figure 5. This entails that the performance of these cells is not limited by the transport of photogenerated carriers, at least for the active layer thickness used here ($L \approx 100$ nm). We observe that at voltages

dx.doi.org/10.1021/jp305941f | J. Phys. Chem. C 2012, 116, 16925–16933

approaching V_{oc}, R_t and R_{rec} exhibit similar values, which suggests that thicker active films would suffer from deficient charge collection as expected for highly recombining cells (i.e., $R_t > R_{rec}$). It is also worth noting that two different kinds of series resistance effects have been identified: one related to the transport processes in conductive materials R_s, and another one associated with the charge transfer events at the outer interfaces between the active layer and the contacts R_{co}. While R_{co} exceeds R_s by more than 1 order of magnitude at low voltages, both resistors contributes similarly to the total series resistance at forward bias near V_{oc}.

As stated in the Introduction, the observation of diffusion of minority carriers through extended neutral regions within the active layer bulk relies on the occurrence of the lifetime semiconductor regime. The blends of donor and acceptor molecules is regarded as an effective semiconducting medium in which holes act as majority carriers. The lifetime regime implies that $\tau_{rec} > \tau_{die}$, and this statement can be confirmed by comparing independent measurements of τ_{rec} using eq 3, and τ_{die} by looking at the first decay characteristic time of light-induced current transients.[13] From C_μ and R_{rec} as shown in Figures 5 and 6, it can be inferred that $\tau_{rec} > 3$ μs. This is a minimum value that is reached at $V_{app} \approx V_{oc}$. A direct determination of the relaxation time τ_{die} results from the exponential response time of current transients presented in Figure 9 for both Ca and CaO cathodes. We systematically

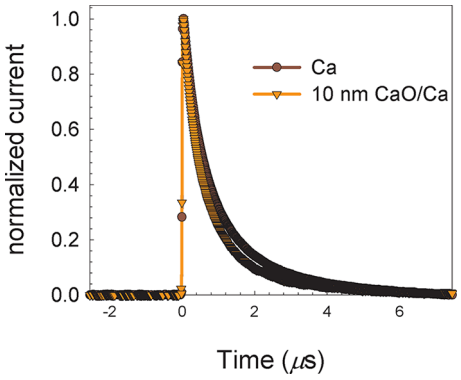

Figure 9. Example of normalized transient photocurrent of P3HT:PCBM devices using blocking and extracting electrodes. The first rapid decay is related to the dielectric relaxation time, which is observed to be within the range of 0.6−0.7 μs.

measured $\tau_{die} \approx 0.65$ μs in good agreement with the estimation proposed in the Introduction. This last finding indicates that P3HT:PCBM blends operate within the relaxation semiconductor regime. Similar to the established distinction between lifetime and relaxation regimes in terms of the response times ($\tau_{rec} > \tau_{die}$), a comparison of characteristic length scales points to the same underlying physics. The diffusion length is defined as an average distance in which mobile carriers can diffuse before recombination, and is related to the diffusion coefficient in eq 4 as follows:

$$L_n = \sqrt{D_n \tau_{rec}} \quad (5)$$

In the time scale of dielectric relaxation the characteristic length scale corresponds to the Debye screening length λ_D that represents the distance in which local electrical fields are confined. It can be demonstrated that an expression as eq 5 results relating λ_D and τ_{die} in such a way that,

$$\lambda_D = \sqrt{D_n \tau_{die}} \quad (6)$$

Thus, the occurrence of the lifetime regime as $L_n > \lambda_D$ in terms of a length scale comparison can be formulated. In the case of the analyzed cells values of $\lambda_D \approx 50$ nm are obtained, whereas L_n ranges from ∼250 nm for low forward voltages down to ∼100 nm at $V_{app} \approx V_{oc}$. It is then deduced that at high voltages L_n is comparable to the active layer thickness. The photovoltaic devices analyzed operating under these conditions are then in the limit of being considered as highly recombining solar cells for which $L \gg L_n$. This last observation explains why thicker films usually exhibit poor performance as bulk transport losses occur before charge collection take place at the contacts. Our analysis offers a straightforward method for complete device performance evaluation.

7. CONCLUSIONS

This work provides a general impedance model that is tested using two extremely different sets of P3HT:PCBM-based devices: reasonably efficient solar cells and devices where the electron collection has been blocked. The first type relies on an efficient collecting Ca cathode and the second on the addition of oxide interlayers (CaO) between the active layer and the cathode contact. The transmission line circuit accounting for the bulk processes is found to be valid irrespective of the structure selected for the cathode contact. It is observed that coupling of diffusion and recombination currents suffices to model electrical mechanisms occurring at the organic blend. The analytical impedance method presented is a tool that allows us to determine and separate different resistive contributions affecting the solar cell operation. By confronting transport (diffusion) resistance to recombination resistance, rapid quantification of carriers lost during the transit to the outer contacts is found. In addition, the effect of the cathode contact is modeled by means of series resistance and capacitance elements, providing further evidence and determination about the important and detrimental effect of contacts. We finally note that the analysis performed here needs to be extended to organic solar cells comprising other blend constituents, particularly different donor polymers, to fully evaluate its application degree.

AUTHOR INFORMATION

Corresponding Author

*Tel.: +34 964 387548; fax: +34 964 729218; e-mail: garciag@fca.uji.es.

Notes

The authors declare no competing financial interest.

ACKNOWLEDGMENTS

We thank financial support from Ministerio de Educacion y Ciencia under project HOPE CSD2007-00007 (Consolider-Ingenio 2010), Generalitat Valenciana (Prometeo/2009/058, ACOMP/2009/056, ACOMP/2009/095, and ISIC/2012/008 Institute of Nanotechnologies for Clean Energies), and FP7 European project ORION (Large CP-IP 229036-2).

REFERENCES

(1) Green, M. A.; Emery, K.; Hishikawa, Y.; Warta, W.; Dunlop, E. D. *Prog. Photovoltaics* **2012**, *20*, 12−20.

(2) Park, S. H.; Roy, A.; Beaupré, S.; Cho, S.; Coates, N.; Moon, J. S.; Moses, D.; Leclerc, M.; Lee, K.; Heeger, A. J. *Nat. Photonics* **2009**, *3*, 297−302.

(3) Boix, P. P.; Guerrero, A.; Marchesi, L. F.; Garcia-Belmonte, G.; Bisquert, J. *Adv. Energy Mater.* **2011**, *1*, 1073−1078.
(4) Peet, J.; Wen, L.; Byrne, P.; Rodman, S.; Forberich, K.; Shao, Y.; Drolet, N.; Gaudiana, R.; Dennler, G.; Waller, D. *Appl. Phys. Lett.* **2011**, *98*, 043301.
(5) Cowan, S. R.; Banerji, N.; Leong, W. L.; Heeger, A. J. *Adv. Funct. Mater.* **2012**, *22*, 1116−1128.
(6) Credgington, D.; Durrant, J. R. *J. Phys. Chem. Lett.* **2012**, *3*, 1465−1478.
(7) Fonash, S. J. *Solar Cell Device Physics*, 2nd ed.; Elsevier: Burlington, 2010.
(8) van Roosbroek, W.; Casey, H. C. *Phys. Rev. B* **1972**, *5*, 2154−2175.
(9) Schiff, E. A. *Sol. Energy Mater. Sol. Cells* **2003**, *78*, 567−595.
(10) Bozano, L.; Carter, A.; Scott, J. C.; Malliaras, G. G.; Brock, P. J. *Appl. Phys. Lett.* **1999**, *74*, 1132−1134.
(11) Gregg, B. A.; Liang, Z. *Adv. Mater.* **2012**, *24*, 3258−3262.
(12) Liang, Z.; Nardes, A.; Wang, D.; Berry, J. J.; Gregg, B. A. *Chem. Mater.* **2009**, *21*, 4914−4919.
(13) Morfa, A. J.; Nardes, A. M.; Shaheen, S. E.; Kopidakis, N.; Lagemaat, J. v. d. *Adv. Funct. Mater.* **2011**, *21*, 2580−2586.
(14) Mozer, A. J.; Sariciftci, N. S. *Chem. Phys. Lett.* **2004**, *389*, 438−442.
(15) Goh, C.; Kline, R. J.; McGehee, M. D.; Kadnikova, E. N.; Fréchet, J. M. J. *Appl. Phys. Lett.* **2005**, *86*, 122110.
(16) Maurano, A.; Hamilton, R.; Shuttle, C. G.; Ballantyne, A. M.; Nelson, J.; O'Regan, B.; Zhang, W.; McCulloch, I.; Azimi, H.; Morana, M.; Brabec, C. J.; Durrant, J. R. *Adv. Mater.* **2010**, *22*, 4987−4992.
(17) Garcia-Belmonte, G.; Boix, P. P.; Bisquert, J.; Sessolo, M.; Bolink, H. J. *Sol. Energy Mater. Sol. Cells* **2010**, *94*, 366−375.
(18) Garcia-Belmonte, G.; Munar, A.; Barea, E. M.; Bisquert, J.; Ugarte, I.; Pacios, R. *Org. Electron.* **2008**, *9*, 847−851.
(19) Bisquert, J.; Garcia-Belmonte, G. *J. Phys. Chem. Lett.* **2011**, *2*, 1950−1964.
(20) Lee, J.; Kong, J.; Kim, H.; Kang, S.-O.; Lee, K. *Appl. Phys. Lett.* **2011**, *99*, 243301.
(21) Li, J. V.; Nardes, A. M.; Liang, Z.; Shaheen, S. E.; Gregg, B. A.; Levi, D. H. *Org. Electron.* **2011**, *12*, 1879−1885.
(22) Burgelman, M.; Grasso, C. *J. Appl. Phys.* **2004**, *95*, 2020.
(23) Bisquert, J. *J. Phys. Chem. B* **2002**, *106*, 325−333.
(24) Ratcliff, E. L.; Zacher, B.; Armstrong, N. R. *J. Phys. Chem. Lett.* **2011**, *2*, 1337−1350.
(25) Guerrero, A.; Marchesi, L. F.; Boix, P. P.; Ruiz-Raga, S.; Ripolles-Sanchis, T.; Garcia-Belmonte, G.; Bisquert, J. *ACS Nano* **2012**, *6*, 3453−3460.
(26) Bisquert, J. *Phys. Chem. Chem. Phys.* **2003**, *5*, 5360−5364.
(27) Xu, H.; Zhang, Z.; Penga, L.-M. *Appl. Phys. Lett.* **2011**, *98*, 133122.
(28) Donolato, C. A *Appl. Phys. Lett.* **1985**, *46*, 270−272.
(29) Fabregat-Santiago, F.; Garcia-Belmonte, G.; Mora-Seró, I.; Bisquert, J. *Phys. Chem. Chem. Phys.* **2011**, *13*, 9083−9118.
(30) Leong, W. L.; Cowan, S. R.; Heeger, A. J. *Adv. Energy Mater.* **2011**, *1*, 517−522.
(31) Zhang, Y.; Dang, X.-D.; Kim, C.; Nguyen, T.-Q. *Adv. Energy Mater.* **2011**, *1*, 610−617.
(32) Leever, B. J.; Bailey, C. A.; Marks, T. J.; Hersam, M. C.; Durstock, M. F. *Adv. Energy Mater* **2012**, *2*, 120−128.
(33) Perrier, G.; deBettignies, R.; Berson, S.; Lemaître, N.; Guillerez, S. *Sol. Energy Mater. Sol. Cells* **2012**, *101*, 210−216.
(34) Pitarch, A.; Garcia-Belmonte, G.; Mora-Seró, I.; Bisquert, J. *Phys. Chem. Chem. Phys.* **2004**, *6*, 2983−2988.
(35) Guerrero, A.; Marchesi, L. F.; Boix, P. P.; Bisquert, J.; Garcia-Belmonte, G. *J. Phys. Chem. Lett.* **2012**, *3*, 1386−1392.
(36) Whited, R. C.; Flaten, C. J.; Walker, W. C. *Solid State Commun.* **1973**, *13*, 1903−1905.
(37) Rekhson, S. M.; Mazurin, O. V. *J. Am. Ceram. Soc.* **1974**, *57*, 327.
(38) Baldo, M. A.; Forrest, S. R. *Phys. Rev. B* **2001**, *64*, 085201.
(39) Bisquert, J. *J. Phys. Chem. B* **2004**, *108*, 2323−2332.
(40) Garcia-Belmonte, G.; Bisquert, J.; Popkirov, G. *Appl. Phys. Lett.* **2003**, *83*, 2178−2180.
(41) Bisquert, J. *Phys. Chem. Chem. Phys.* **2008**, *10*, 3175−3194.
(42) Mihailetchi, V. D.; van Duren, J. K. J.; Blom, P. W. M.; Hummelen, J. C.; Janssen, R. A. J.; Kroon, J. M.; Rispens, M. T.; Verhees, W. J. H.; Wienk, M. M. *Adv. Funct. Mater.* **2003**, *13*, 43−46.